Experimental and Mechanistic Understanding of Aldehyde Hydrogenation Using Au$_{25}$ Nanoclusters with Lewis Acids: Unique Sites for Catalytic Reactions

Gao Li,[†,§] Hadi Abroshan,[‡,§] Yuxiang Chen,[‡] Rongchao Jin,*[,‡] and Hyung J. Kim*[,‡,#]

[†]State Key Laboratory of Catalysis & Gold Catalysis Research Centre, Dalian Institute of Chemical Physics, Chinese Academy of Sciences, Dalian 116023, China

[‡]Department of Chemistry, Carnegie Mellon University, Pittsburgh, Pennsylvania 15213, United States

[#]School of Computational Sciences, Korea Institute for Advanced Study, Seoul 130-722, Korea

S *Supporting Information*

ABSTRACT: The catalytic activity of Au$_{25}$(SR)$_{18}$ nanoclusters (R = C$_2$H$_4$Ph) for the aldehyde hydrogenation reaction in the presence of a base, e.g., ammonia or pyridine, and transition-metal ions M^{z+}, such as Cu$^+$, Cu^{2+}, Ni^{2+} and Co^{2+}, as a Lewis acid is studied. The addition of a Lewis acid is found to significantly promote the catalytic activity of Au$_{25}$(SR)$_{18}$/CeO$_2$ in the hydrogenation of benzaldehyde and a number of its derivatives. Matrix-assisted laser desorption ionization (MALDI) and electrospray ionization (ESI) mass spectrometry in conjunction with UV−vis spectroscopy confirm the generation of new species, Au$_{25-n}$(SR)$_{18-n}$ (n = 1−4), in the presence of a Lewis acid. The pathways for the speciation of Au$_{24}$(SR)$_{17}$ from its parent Au$_{25}$(SR)$_{18}$ nanocluster as well as its structure are investigated via the density functional theory (DFT) method. The adsorption of M^{z+} onto a thiolate ligand "—SR—" of Au$_{25}$(SR)$_{18}$, followed by a stepwise detachment of "—SR—" and a gold atom bonded to "—SR—" (thus an "Au-SR" unit) is found to be the most likely mechanism for the Au$_{24}$(SR)$_{17}$ generation. This in turn exposes the Au$_{13}$-core of Au$_{24}$(SR)$_{17}$ to reactants, providing an active site for the catalytic hydrogenation. DFT calculations indicate that M^{z+} is also capable of adsorbing onto the Au$_{13}$-core surface, producing a possible active metal site of a different kind to catalyze the aldehyde hydrogenation reaction. This study suggests, for the first time, that species with an open metal site like adducts [nanoparticle-M]$^{(z-1)+}$ or fragments Au$_{25-n}$(SR)$_{18-n}$ function as the catalysts rather than the intact Au$_{25}$(SR)$_{18}$.
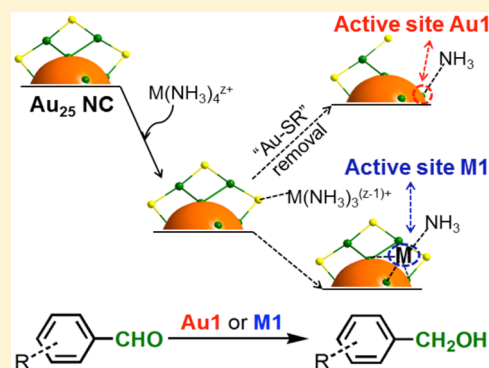
INTRODUCTION

Over the past decade, atomically precise gold nanoclusters have emerged as a novel and promising nanomaterial in nanoscience and nanotechnology.[1−3] Due to their unique catalytic properties for a wide range of different reactions, such as oxidation, hydrogenation, and carbon−carbon coupling reactions, to name a few,[4−9] they have gained overwhelming research interests. Compared to conventional gold nanocatalysts (for example, naked nanoparticles) with unknown surface structure, these gold nanoclusters are characterized by well-defined frameworks,[3] e.g., [Au$_{25}$(SR)$_{18}$]$^−$[TOA]$^+$ (SR = thiolate ligands, TOA = tetraoctylammonium), so that they provide an excellent arena to investigate how the atomic structure and their catalytic properties are related, especially from the reaction mechanisms point of view. Specifically, [Au$_{25}$(SR)$_{18}$]$^−$[TOA]$^+$ (or simply Au$_{25}$(SR)$_{18}$) nanoclusters are composed of a 13-atom icosahedral core (Au$_{13}$) and six staple shell motifs Au$_2$(SR)$_3$ ("—SR—Au—SR—Au—SR—", see Figure S1 in the Supporting Information). These nanoparticles enable a detailed analysis via quantum chemistry methods to understand the catalytic reactions.[10,11] On the basis of DFT calculations, the

Au$_3$ sites (Figure S1) or the staple motifs of the Au$_{25}$(SR)$_{18}$ nanoclusters are usually deemed as catalytically active sites in the catalytic reactions.[12,13] For instance, DFT predicts that both phenylacetylene and iodobenzene molecules are adsorbed on a Au$_3$ site of the Au$_{25}$(SR)$_{18}$ nanoclusters in the Sonogashira cross-coupling reaction.[11] By contrast, the Au$_{13}$ icosahedral core would not be able to bind directly to the reactants in the catalytic reactions despite its strong electronic influence on the staple motifs and Au$_3$ sites.[10,14,15]

Recently, nanogold catalysts have been widely applied in the hydrogenation reactions.[16−21] In their recent study of chemoselective hydrogenation of nitrobenzaldehyde to nitrobenzyl alcohol, Jin and co-workers were able to achieve the catalytic performance of a series of Au$_n$(SR)$_m$ nanoclusters (where n and m varied from 15 to 99 and from 14 to 42, respectively) with ∼100% selectivity using H$_2$ gas as the hydrogen source and pyridine as the base in both homogeneous and heterogeneous catalytic systems.[13,22] DFT calculations indicated that both the

—CHO and —NO$_2$ groups of the reactant interact strongly with the "—SR—Au—SR—" staples on the Au$_n$(SR)$_m$ nanoclusters; the adsorption energy of the nitrobenzaldehyde on the Au$_{25}$(SCH$_3$)$_{18}^-$ nanocluster is ~ −1.03 eV (here and hereafter, a negative value means a favorable interaction).[13] It should be noted that there has been a significant effort to develop transition metal complexes for efficient C=O bond hydrogenation.[23−26] Despite their high performance, however, catalytic active sites were reported to be difficult to generate. In view of this challenge as well as several disadvantages of homogeneous catalysis, including the poor catalyst recovery and the difficulty of removing catalysts from the products, it is desirable to develop heterogeneous catalysis. The advantages include excellent recyclability of catalysts, easy separation of products, and better thermal stability.

Lewis acid, e.g., transition metal ions M^{z+}, is known to promote gold nanoparticle-catalyzed reactions.[27,28] For example, the hydrogenation rate and allylic alcohol chemoselectivity were found to improve in the presence of Co^{2+} for the chemoselective hydrogenation of α,β-unsaturated carbonyl compounds, catalyzed by PVP-protected Au^0 nanoparticles (PVP = polyvinylpyrrolidone).[27] Despite its widespread use as a promoter in the catalytic reactions, however, the mechanism for the promotion via Lewis acid is still not known. Thus, it would be extremely worthwhile to investigate the molecular details of its role in the hydrogenation reactions.

In this article, we report on the Lewis acid-promoted hydrogenation of aldehyde to alcohol catalyzed by Au$_{25}$(SR)$_{18}$/CeO$_2$ (hereafter, SR = SC$_2$H$_4$Ph) in the presence of a base (pyridine or NH$_3$·H$_2$O) under mild conditions (18 bar H$_2$ at 323 K). By monitoring the reaction media using UV−vis spectroscopy in conjunction with MALDI and ESI mass spectrometry, we have found that Au$_{25}$(SR)$_{18}$ nanoclusters undergo detachment of SR ligands and Au atoms in the presence of a Lewis acid, resulting in the formation of Au$_{25-n}$(SR)$_{18-n}$ (n = 1−4) species with catalytic active sites for the aldehyde-to-alcohol hydrogenation. Possible configurations of Au$_{24}$(SR)$_{17}$ are examined using the DFT and time-dependent DFT (TD-DFT) methods. Our calculations indicate that the catalytic active site located on the Au$_{13}$-core of Au$_{24}$(SCH$_3$)$_{17}$ is capable of activating the covalent bond of H$_2$ heterolytically, leaving H$^-$ on the core for the ensuing hydrogenation. To our knowledge, this is the first report with convincing experimental and theoretical evidence that the Au$_{13}$-core is responsible for the catalytic reactions.

■ EXPERIMENTAL SECTION

Chemicals. Methylene chloride (HPLC grade, 99.9%, Sigma−Aldrich), ammonium hydroxide (99%, Sigma−Aldrich), ceria (99%, Sigma−Aldrich), pyridine (99%, Sigma−Aldrich), methanol (absolute, 200 proof, Pharmco), Co(OAc)$_2$ (99.99%, Sigma−Aldrich), Cu-(OAc)$_2$ (99.99%, Sigma−Aldrich), Cu(OAc)$_1$ (97%, Sigma−Aldrich), Cu(NO$_3$)$_2$ (purum p.a., 98.0−103% (RT), Sigma−Aldrich), and NiCl$_2$ (98%, Sigma−Aldrich), Cr(NO$_3$)$_3$ (99.0%, Sigma−Aldrich). All chemicals were used as received. Nanopure water (resistivity 18.2 MΩ·cm) was purified with a Barnstead NANOpure Diwater system. All glassware was thoroughly cleaned with aqua regia (HCl:HNO$_3$ = 3:1 vol %), rinsed with copious Nanopure water, and then dried in an oven prior to use.

Characterization. UV−vis spectra were acquired on a Hewlett-Packard (HP) Agilent 8453 diode array spectrophotometer at room temperature. MALDI-MS was performed with a PerSeptiveBiosystems Voyager DE super-STR time-of-flight (TOF) mass spectrometer. Trans-2-[3-(4-*tert*-butylphenyl)-2-methyl-2-propenyldidene]-malononitrile (DCTB) was used as the matrix in MALDI analysis. The nanoclusters and the matrix were dissolved in dichloromethane and then spotted onto the steel plate and dried in vacuum prior to MALDI analysis. ^{1}H NMR was run on a Bruker 300 MHz spectrometer. Electrospray ionization (ESI) mass spectra were obtained using a Waters Q-TOF mass spectrometer equipped with a Z-spray source. The sample was dissolved in toluene (1 mg/mL) and then mixed with a dry methanol solution of CH$_3$CO$_2$Cs (50 mM) by a 1:1 vol ratio. Thermogravimetric analysis (TGA) was conducted with a ~1 mg Au$_{25}$(SR)$_{18}$ sample under N$_2$ atmosphere (flow rate 50 mL/min) on a TG/DTA 6300 analyzer (Seiko Instruments, Inc.), and the temperature was maintained at 150 °C for 60 min. Fourier-transform infrared (FT−IR) measurements were recorded on a Brukers/Tensor 27 instrument (resolution, 1 cm^{-1}; scans, 8; range, 1000−4000 cm^{-1}).

Immobilization of the Au$_{25}$(SR)$_{18}$ Nanoclusters on CeO$_2$ Supports. The CeO$_2$ oxide is chosen as the support for Au$_{25}$(SR)$_{18}$ nanoclusters. According to a previous work by Li et al., CeO$_2$ can lead to a higher catalytic efficiency of the supported nanoclusters than other oxide-supports (e.g., TiO$_2$, SiO$_2$) in the catalytic hydrogenation reaction.[22] For immobilization of nanoclusters Au$_{25}$(SR)$_{18}$, typically, 10 mg [Au$_{25}$(SR)$_{18}$]$^-$[TOA]$^+$ nanoclusters were dissolved in 30 mL dichloromethane, and 1g CeO$_2$ was added. After stirring for 6h at r.t., the Au$_{25}$(SR)$_{18}$/CeO$_2$ catalysts were collected by centrifugation and dried in vacuum. The catalysts were then annealed at 423 K for ~1 h in a vacuum oven. It has been proven previously that Au$_{25}$(SR)$_{18}$ nanoclusters loading on the oxides after the thermal treatment (423 K) is intact.[8,12]

Typical Procedure for the Hydrogenation Reaction. In a typical hydrogenation reaction, benzaldehyde (0.1 mmol), ammonium hydroxide (5 μL), Au$_{25}$(SR)$_{18}$/CeO$_2$ (100 mg, 1 wt % loading of Au$_{25}$(SR)$_{18}$), M^{z+} salt (promoter, 0.14 μmol), and 1 mL water were added to a reactor (Parr instrument company, 22 mL capacity, series 4700) and gaseous H$_2$ was introduced until 18 bar. The reaction temperature was kept at 323 K for 10 h. After the catalytic reaction, the catalyst was separated by centrifugation (~1000 rpm, 1 min). Then the supernatant was extracted by ethyl acetate, and the product was obtained by the solvent removing. The conversion of aldehyde was determined by ^{1}H NMR analysis. In recycling reaction tests, the catalyst was collected by centrifugation (4000 rpm) for 2 min after the reaction. Next, the catalyst was washed with water and acetone to remove the salts and other complexes, and dried in vacuum. The catalyst thus prepared was then reused in a fresh reaction medium with no M^{z+} salt added.

Computational Details. DFT optimization was performed using the B3PW91 hybrid density functional. The 6-31G** basis set was employed for H, C, N, O, and S,[29−32] while the valence aug-cc-pVDZ basis set together with the appropriate Stuttgart-Dresden effective core potentials (ECPs) was used for transition metal ions, Cu$^+$, Cu^{2+}, Ni^{2+}, and Co^{2+}.[33−35] For gold atoms, the LANL2DZ basis set was used.[36] The B3PW91 functional with the LANL2DZ basis set has been shown to predict accurately the structure of Au nanoclusters.[37−40] The reaction energy is determined as the energy difference $\Delta E = \Sigma E_{pro} - \Sigma E_{rea}$, where ΣE_{pro} and ΣE_{rea} are total energies of the products and reactants, respectively. The integral equation formalism polarizable continuum model (IEFPCM) was applied to study the solvation effect on reaction energetics.[41] TD-DFT calculations of optical absorption spectra were also performed and compared with experimental UV−vis results. All calculations were carried out with the Gaussian09 package.[32]

■ RESULTS AND DISCUSSION

Characterization of the Au$_{25}$(SR)$_{18}$/CeO$_2$ Catalyst. Previous studies showed that the Au$_{25}$(SR)$_{18}$ nanoclusters are stable under the conditions of 20 bar of hydrogen at 80 °C.[22] Since the reaction condition employed in our current study (18 bar at 50 °C) is milder than the earlier cases, the clusters are believed to be stable in our case as well. Isothermal stability analysis of the unsupported Au$_{25}$(SR)$_{18}$ nanoclusters showed no discernible loss of ligands during the isothermal process

(Figure S2), suggesting that the thermal treatment (at 150 °C in a N_2 atmosphere) does not induce the ligand loss. Further, the FT−IR analysis was performed for the $Au_{25}(SR)_{18}/CeO_2$ catalyst before and after the 150 °C treatment in vacuum and in an O_2 atmosphere (1 bar). Prior to the FT−IR measurements, the samples were washed after the thermal treatment using pure ethanol three times and dried in vacuum at room temperature. The FT−IR spectra of the sample before and after the treatment in vacuum are superimposable (Figure S3), strongly indicating that the $Au_{25}(SR)_{18}$ nanoclusters on the surface of CeO_2 indeed remain intact. These results are fully consistent with previous work by Jin and co-workers.[8,12] By contrast, the sample treated in O_2 shows ligand loss during the thermal treatment (Figure S4), in good agreement with previous study.[42]

Catalytic Performance of the $Au_{25}(SR)_{18}$ Nanocluster with Lewis Acids in the Chemoselective Hydrogenation of 4-Nitrobenzaldehyde. The results for the catalytic efficiency of gold nanoclusters in the absence and presence of different Lewis acids, viz., transition metal ions, Co^{2+}, Ni^{2+}, Cu^+, Cu^{2+}, and Cr^{3+}, under otherwise the same reaction conditions are compared in Table 1. Several aspects are noteworthy. First,

Table 1. Influence of Different Lewis Acids ($M^{z+}X_z$) on the Chemoselective Hydrogenation of 4-Nitrobenzaldehyde (1) to 4-Nitrobenzyl Alcohol (2) Catalyzed By $Au_{25}(SR)_{18}/CeO_2$.[a]
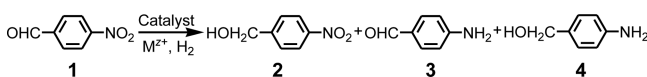
entry	catalyst	M^{z+}	conv. [%][b]	selectivity [%][b]		
				2	3	4
1	$Au_{25}(SR)_{18}$		13.4	∼100		
2	$Au_{25}(SR)_{18}$	$Co(OAc)_2$	90.1	∼100		
3	$Au_{25}(SR)_{18}$	$Cr(NO_3)_3$	75.8	∼100		
4	$Au_{25}(SR)_{18}$	$NiCl_2$	78.2	∼100		
5	$Au_{25}(SR)_{18}$	$Cu(OAc)_1$	61.1	∼100		
6	$Au_{25}(SR)_{18}$	$Cu(OAc)_2$	50.0	∼100		
7	$Au_{25}(SR)_{18}$	$Cu(NO_3)_2$	50.8	∼100		
8	$Au_{25}(SR)_{18}$	$CoCl_2$	90.8	∼100		
9		$Co(OAc)_2$	n.r.			
10	$Au_{25}(SR)_{18}$[c]	$Co(OAc)_2$	82.5	>99.5		
11	$[Au_{25}Co]$[d]		87.3	∼100		
12	$[Au_{25}Co]$[e]		88.4	∼100		

[a]Reaction conditions: 100 mg $Au_{25}(SR)_{18}/CeO_2$ catalyst (∼1 wt % $Au_{25}(SR)_{18}$ loading) in 1 mL water, $M^{z+}/Au_{25}(SR)_{18}$ = 2:1 (mol/mol), 0.1 mmol 4-nitrobenzaldehyde, 5 μL pyridine, 18 bar H_2 at 323 K, 10 h. [b]The conversion (conv.) of 4-nitrobenzaldehyde and selectivity were determined by ^1H NMR spectrum. n.r. = no reaction. [c]Reaction conditions: 4 g $Au_{25}(SR)_{18}/CeO_2$ catalyst (∼40 mg $Au_{25}(SR)_{18}$ loading) in 30 mL water, 1.05 mmol $Co(OAc)_2$, 5 mmol 4-nitrobenzaldehyde, 300 μL pyridine, 18 bar H_2 at 323 K, 10 h. [d]2nd and [e]3rd reuses of the catalyst recovered from entry 2. [d,e]No M^{z+} was added to the reaction system.

in the absence of a Lewis acid, $Au_{25}(SR)_{18}/CeO_2$ catalyst yields a very low conversion at 323 K (13.4%, Table 1, entry 1). When the temperature is raised to 353 K, however, the conversion can reach ∼93% as reported previously.[22] As mentioned above, in this work, the temperature was kept at 323 K to investigate the effects of the Lewis acids. Second, the conversion improves markedly to 90.1% and the turnover frequency (TOF = [reacted mol of aldehyde]/[(mol of Au clusters) × (reaction

time)]) reaches 70.8 h^{-1} when $Co(OAc)_2$ is added (molar ratio of Co^{2+}: $Au_{25}(SR)_{18}$ = 2:1) (Table 1, entry 2). We note that this level of promotion exceeds the 73.2% conversion obtained with Au/PVP nanoparticles with the same Co^{2+} in earlier studies.[22,27] Other transition-metal ions result in the catalytic efficiency enhancement of $Au_{25}(SR)_{18}/CeO_2$ to a varying degree. Specifically, moderate to significant conversions (50.0 to 78.2%) are achieved with Ni^{2+}, Cr^{3+}, Cu^+, and Cu^{2+}. The degree of promotion of the catalytic activity of $Au_{25}(SR)_{18}/CeO_2$ by M^{z+} is in the order $Co^{2+} > Ni^{2+} ≈ Cr^{3+} > Cu^+ > Cu^{2+}$. Third, near 100% chemoselectivity for the alcohol product was observed in all the catalytic reactions (Table 1). It should be noted that no conversion was detected in the case of blank experiments in which $Au_{25}(SR)_{18}$ nanoclusters are absent and only Lewis acid and CeO_2 oxide are present (Table 1, entry 9 and Table S1). This confirms that catalytic activity arises from the gold nanoclusters.

To shed additional light on roles of M^{z+}, we studied the catalytic activity of the *unsupported* $Au_{25}(SR)_{18}$ in the presence and absence of $Co(OAc)_2$. The reaction conditions were: 0.13 μmol unsupported nanoclusters, 0.26 μmol $Co(OAc)_2$ (if used) in 1 mL of toluene/ethanol (1:1, v/v), 0.1 mL of H_2O, 0.1 mmol 4-nitrobenzaldehyde, 5 μL pyridine, and 18 bar H_2 at 323 K for 10 h. The unsupported catalysts yielded, respectively, 17.9% and 1.3% conversion with 100% selectivity toward alcohol product in the presence and absence of the Lewis acid. These results strongly support that the Lewis acid is indeed a promoter. Also notable is that the conversion rate of the unsupported catalysts is considerably lower than the supported ones. Two aspects are worthy of note here: First, metal oxides are commonly used to disperse and stabilize nanoparticles and to promote the reactions in heterogeneous catalysts.[43,44] The nature of the catalyst's support can play a crucial role in the catalytic activity of the nanoparticles. Despite extensive efforts, however, the details of the interactions of the particles and the supports still remain elusive due to the complexity of the systems. Nonetheless, the high activity of gold nanoparticles on CeO_2 is often attributed to the excellent redox properties of ceria which lead to easy formation and diffusion of oxygen defects.[45] Second, because of the low solubility of the catalyst in polar solvents, we conducted the reactions with the unsupported catalyst in a solvent mixture (1 mL of toluene/ethanol (1:1, v/v) + 0.1 mL of H_2O) that is considerably less polar than water used in the supported case. According to the hydrogenation mechanisms proposed below, solvation can play an important role by facilitating (or even inducing) the elongation of the H—H bond of H_2. Therefore, lowering the solvent polarity would result in the deceleration of the heterolytic bond cleavage of H_2 and thus of the aldehyde-to-alcohol conversion.

Another important aspect of our results in Table 1 is that anions do not play any significant role in the hydrogenation reaction. As presented in entries 6 and 7, copper salts with different anions, $Cu(NO_3)_2$ and $Cu(OAc)_2$, yield essentially the same conversion rate (50.0 vs 50.8%). The cobalt salts, $Co(OAc)_2$ and $CoCl_2$, show the same behavior (entries 2 and 8). These results strongly suggest that the anions act merely as a spectator.

To gain insight into the performance of the catalyst in large scale synthesis, we scaled up the catalytic system and examined reaction kinetics under the conditions as indicated in Table 1. The conversion rate and selectivity for the alcohol product for this scaled-up system were found to be 82.5% and 99.5%,

respectively (Table 1, entry 10). These results are close to those reported as entry 2 of Table 1 for the smaller scale catalysis (90.1% and 100%, respectively). Therefore, $Au_{25}(SR)_{18}/CeO_2$ in the presence of $Co(OAc)_2$ appears to have good potential as a catalyst for large scale synthesis.

We investigated hydrogenation of benzaldehyde and its derivatives to study the influence of substitution. The results obtained in the presence of $Co(OAc)_2$ and pyridine are compiled in Table 2. The conversion of unsubstituted

Table 2. Hydrogenation of a Range of Substrates with Nitro and Aldehyde Groups over $Au_{25}(SR)_{18}/CeO_2$ in the Presence of $Co(OAc)_2$ Salt^a

Entry	Substrate	Product	Conv. (%)
1	OHC–C₆H₅	HOH₂C–C₆H₅	51.4
2	OHC–C₆H₄–I	HOH₂C–C₆H₄–I	46.5
3	OHC–C₆H₄–CH₃	HOH₂C–C₆H₄–CH₃	37.7
4	OHC–C₆H₄–SCH₃	HOH₂C–C₆H₄–SCH₃	26.8
5	OHC–C₆H₄–NO₂	HOH₂C–C₆H₄–NO₂	90.1
6	o-OHC, O₂N–C₆H₄	o-HOH₂C, O₂N–C₆H₄	21.3
7	OHC–C₆H₄–NO₂ (meta)	HOH₂C–C₆H₄–NO₂ (meta)	91.5

^{a}Reaction conditions: the same as noted in Table 1.

benzaldehyde was found to be 51.4% (Table 2, entry 1). The substitution with a methyl or a methylthio group exerts a considerable influence on the hydrogenation reaction as the conversion of the aldehydes with these substituents decreases to 37.7 and 26.8%, respectively (Table 2, entries 3 and 4). An iodo group has a similar but lesser effect (Table 2, entry 2). Such a decrease in the conversion efficiency is expected because these substituents (methyl, methylthio, and iodo groups) at the para-position are electron donating groups and therefore tend to lower the electron affinity of the carbonyl group of aldehydes toward reduction to alcohol. We also examined the effect of the position of substitution, viz., a nitro group at the ortho-, meta-, and para-positions (Table 2, entries 5–7). The substitution at the meta- or para-position increased the reaction conversion to ~90%. Since the nitro group is an electron withdrawing group, it increases the electron affinity and thus reactivity of the carbonyl group toward reduction to alcohol. However, the substitution at the ortho-position (o-nitrobenzaldehyde) led to the lowest conversion among the three nitrobenzaldehyde reactants (Table 2, entries 5–7). Possible reasons include the intramolecular interactions between two closely located nitro and carbonyl groups and steric hindrance arising from the nitro

group (Figure S5). In such a case, one may be able to improve the reaction conversion by increasing the activity of the reducing agent. Indeed the conversion of o-nitrobenzaldehyde improves markedly to 97.1% when ammonia (NH_3) is used as the base instead of pyridine (Table S2).

To assess the recyclability of the gold nanocluster catalysts, we examined the catalytic activity of the reused $[Au_{25}(SR)_{18}/CeO_2 + Co^{2+}]$ catalyst (collected from entry 2 of Table 2) in the hydrogenation reaction of 4-nitrobenzaldehyde. The catalyst was recovered after the reaction by centrifugation (4000 rpm), washed with water and acetone, and then dried in vacuum. By using the recycled catalyst thus prepared, a fresh reaction was run with reactants in a fresh solvent under identical reaction conditions but in the absence of Lewis acids. The recycled catalyst showed nearly the same activity and selectivity as the fresh catalyst; it yielded 87.3% conversion for the second cycle and 88.4% for the third cycle (Table 1, entries 9 and 10). Since no appreciable loss of catalytic activity and selectivity was observed after 3 cycles (higher cycles were not tested), we conclude that the $[Au_{25}(SR)_{18}/CeO_2 + Co^{2+}]$ catalyst is characterized by a good recyclability in hydrogenation reaction.

We now proceed to examine catalytic mechanisms for hydrogenation. The fact that the presence of M^{z+} ions improves catalytic properties of the nanoclusters indicates that Lewis acids play an important role. We consider two different possible mechanisms for this promotion: (1) parts of the nanocluster surface, such as "—SR—" and "—Au—SR—" units, are removed so that gold atoms of the nanoclusters become exposed/reactive to the reactants; (2) the Lewis acid is adsorbed onto the $Au_{25}(SR)_{18}$ nanoclusters, thereby providing a new active site on the nanoclusters for the reaction.

Characterization of the $Au_{25-n}(SR)_{18-n}$ ($n = 1-4$) species. To gain insight into how Lewis acids promote the hydrogenation reaction, we studied unsupported $Au_{25}(SR)_{18}$ nanoclusters in the presence and absence of a Lewis acid in solution. The unsupported nanoclusters can be easily characterized by UV–vis, MALDI–MS, and ESI–MS. In Figure 1A, UV–vis spectra of two different solutions are displayed: (i) a solution (dichloromethane/methanol 1:1, v/v) of $Au_{25}(SR)_{18}$ nanoclusters in the presence of only ammonia at room temperature, and (ii) the same solution but in the presence of both ammonia and $Co(OAc)_2$ string for 10 h under the same conditions. We note that the acid and $Au_{25}(SR)_{18}$ concentrations, $Co^{2+}:Au_{25}(SR)_{18} = 2:1$ (mol/mol), employed here for UV–vis and MS analysis of unsupported nanoclusters are the same as those used in the hydrogenation reaction study with supported nanoclusters above (Table 1). Comparison of the optical spectra of the two solutions shows that the nanoclusters undergo structural changes when $Co(OAc)_2$ is added. For further insight, we performed MADLI–MS analysis. The results are shown in Figure 1B. Solution i (black line) is characterized by two peaks, which are assigned to $Au_{25}(SR)_{18}$ (m/z: 7394.3, theoretical m/z: 7394.2) and its fragment $Au_{21}(SR)_{14}$ (m/z: 6058.1, theoretical m/z: 6057.4) caused by MADLI-MS. In the case of solution ii (red line), the main peak centered at m/z 7060.3 is assigned to $Au_{24}(SR)_{17}$ (theoretical m/z: 7060.0). Since $Au_{24}(SR)_{17}$ is not formed during the MADLI–MS analysis as evidenced by the result for solution i, it is the presence of Lewis acid that leads to the generation of $Au_{24}(SR)_{17}$ from its parent $Au_{25}(SR)_{18}$ nanoclusters. Nevertheless, some $Au_{25}(SR)_{18}$ are still present as indicated by the much less intense peak at $m/z = 7394.3$.
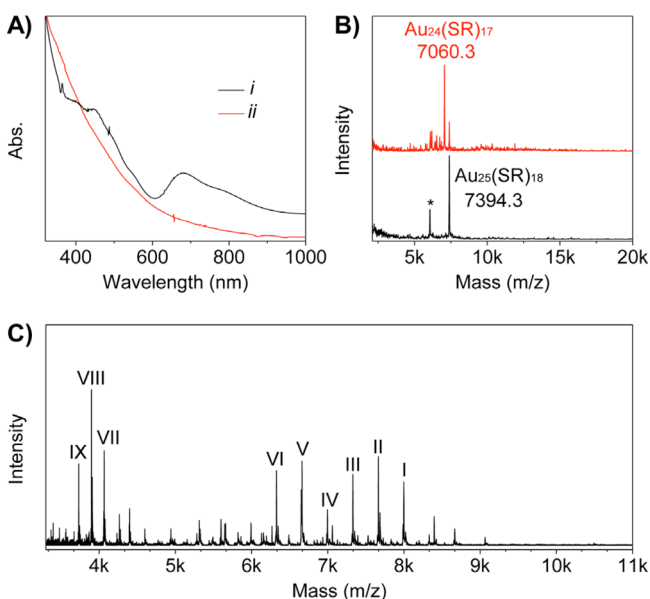
Figure 1. (A) UV–vis and (B) MALDI mass spectra of $Au_{25}(SR)_{18}$ nanoclusters at room temperature stirring for 10 h in a mixed dichloromethane/methanol solution: (i) in the presence of only ammonia (black line), and (ii) in the presence of $Co(OAc)_2$ (Co^{2+}:$Au_{25}(SR)_{18}$ = 2:1, mol/mol) and ammonia (red line). The peak marked with an asterisk (*) is the fragment $Au_{21}(SR)_{14}$ caused by MALDI, rather than an impurity. (C) Positive mode ESI mass spectrum of $Au_{25}(SR)_{18}$ nanoclusters in the presence of $Co(OAc)_2$ (Co^{2+}:$Au_{25}(SR)_{18}$ = 2:1, mol/mol) and pyridine.

For additional information, a sample of $Au_{25}(SR)_{18}$ nanoclusters with $Co(OAc)_2$ (Co^{2+}:$Au_{25}(SR)_{18}$ = 2:1, mol/mol) and pyridine was characterized by the ESI–MS method. ESI–MS is much softer than the MALDI analysis and typically does not cause fragmentation of nanoclusters. Several peaks were observed in the ESI mass spectrum of the sample (Figures 1C and S6). The spacing of the isotope patterns of the peaks I to VI and VII to IX is 1 and 0.5 (Figure S7), respectively. This

indicates that ions I–VI and VII-IX carry 1+ and 2+ charges, respectively. The peak assignments are as follows: peak I at m/z = 7997.87 is assigned to $[Au_{25}(SC_2H_4Ph)_{18}Co_4Py_3Cs]^+$ (theoretical m/z: 7999.70), peak II at 7663.87 to $[Au_{25}(SC_2H_4Ph)_{18}CoPyCs]^+$ (theoretical m/z: 7664.66), peak III at 7328.91 to $[Au_{24}(SC_2H_4Ph)_{17}CoPyCs]^+$ (theoretical m/z: 7329.80), peak IV at 6994.94 to $[Au_{23}(SC_2H_4Ph)_{16}CoPyCs]^+$ (theoretical m/z: 6995.79), peak V at 6660.93 to $[Au_{22}(SC_2H_4Ph)_{15}CoPyCs]^+$ (theoretical m/z: 6660.78), peak VI at 6326.86 to $[Au_{21}(SC_2H_4Ph)_{14}CoPyCs]^+$ (theoretical m/z: 6327.79), peak VII at 4065.40 to $[Au_{25}(SC_2H_4Ph)_{18}Co_4Py_3Cs_2]^{2+}$ (theoretical m/z: 4066.30), peak VIII at 3898.40 to $[Au_{25}(SC_2H_4Ph)_{18}CoPyCs_2]^{2+}$ (theoretical m/z: 3898.36), and peak IX at 3731.42 to $[Au_{24}(SC_2H_4Ph)_{17}CoPyCs_2]^{2+}$ (theoretical m/z: 3731.35). Their experimental isotopic patterns match very well with the simulated ones (Figure S6). Of note, the CoPy adduct appearing in the ESI spectrum was not detected in the MALDI mass spectra as the latter is a "hard" ionization method.

The MALDI and ESI results suggest that both possibilities mentioned above—i.e., removal of "—Au—SR—" units of the staple motif on $Au_{25}(SR)_{18}$ nanoclusters and generation of the adduct from $Au_{25-n}(SR)_{18-n}$ in the presence of Lewis acid (e.g., Co^{2+} ion) and base—can provide mechanistic explanations for catalytic promotion.

We monitored the removal of a "—Au—SR—" unit of $Au_{25}(SR)_{18}$ nanoclusters in the presence of a Lewis acid using UV–vis and MALDI–MS (Figure 2). We first studied the dichloromethane/methanol mixed solution of $Au_{25}(SR)_{18}$ nanoclusters and the $Co(OAc)_2$ salt (Co^{2+}:$Au_{25}(SR)_{18}$ = 2:1, mol/mol) at room temperature (Figure 2A). We observed that the distinct peak at 670 nm gradually decreased, indicating that the $Au_{25}(SR)_{18}$ nanoclusters are slowly converted to other nanoclusters ($Au_{25-n}(SR)_{18-n}$). To understand the influence of the base, we repeated the same experiment but with ammonia added to the system (all other experimental conditions remained the same). Similar to the case of no ammonia (Figure 2A), the UV–vis signature of $Au_{25}(SR)_{18}$ decays but
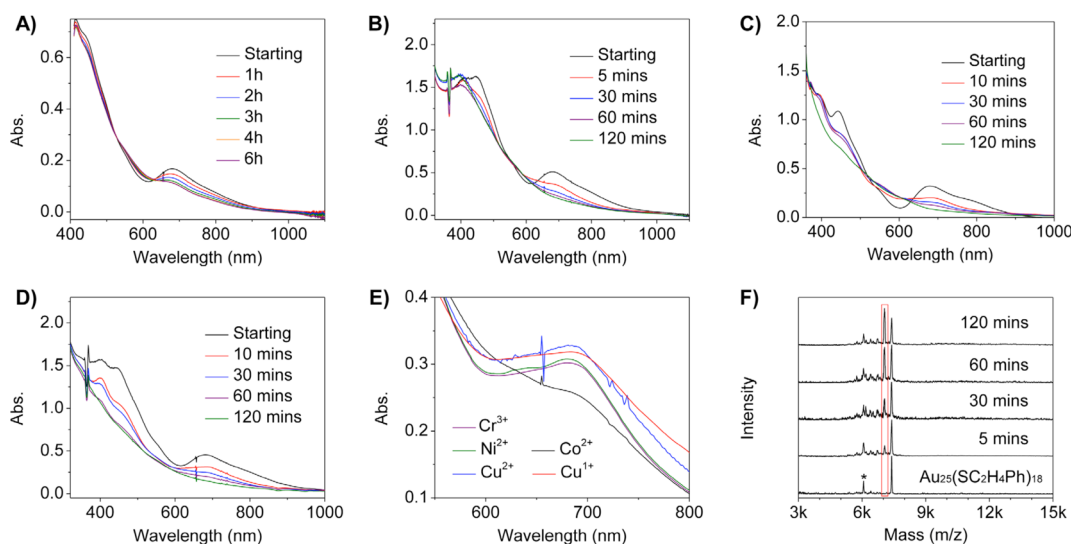

Figure 2. UV–vis spectra tracing of a methanol solution of $Au_{25}(SR)_{18}$ nanoclusters in the presence of (A) only $Co(OAc)_2$, (B) $Co(OAc)_2$ and ammonia, (C) $NiCl_2$ and ammonia, and (D) $Cu(OAc)_2$ and ammonia. (E) UV–vis spectra of $Au_{25}(SR)_{18}$ with $M^{z+}X_z$ at 10 min (and at 5 min in the case of $Co(OAc)_2$). (F) MALDI mass spectra of the $Au_{25}(SR)_{18}$ nanoclusters in the presence of $Cu(OAc)_2$ and ammonia. In all cases, M^{z+}:$Au_{25}(SR)_{18}$ = 2:1 (mol/mol). In (F), the peak marked with an asterisk (*) is a fragment caused by MALDI, rather than an impurity.
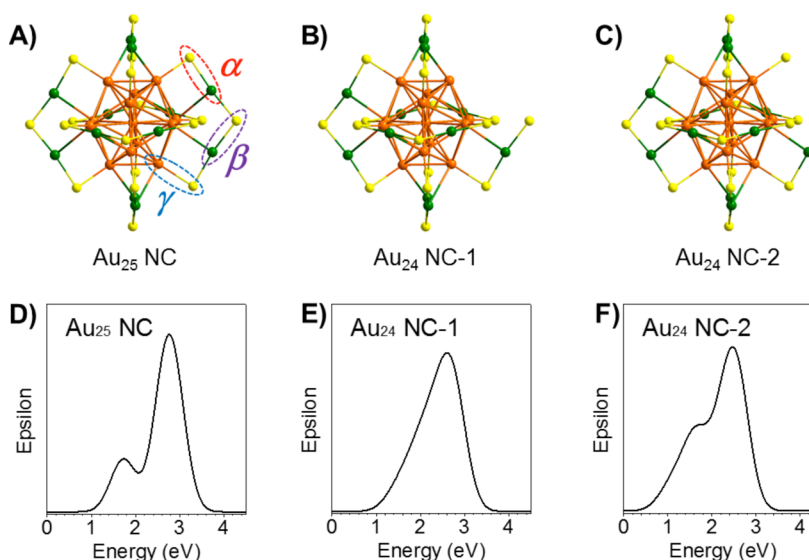
Figure 3. (A) Framework of $Au_{25}(SR)_{18}$ nanoclusters (Au_{25} NC) based on the results of ref 10 and three different "—Au—SR—" fragments (denoted as Au—S: α,β,γ) for possible removal. Detachment of fragments α and β results in $Au_{24}(SR)_{17}$ with configurations (B) Au_{24} NC-1 and (C) Au_{24} NC-2, respectively. Theoretical absorption spectra of $Au_{25}(SCH_3)_{18}^-$ and $Au_{24}(SCH_3)_{17}^-$ in configurations Au24 NC-1 and Au24 NC-2 are presented in (D), (E), and (F), respectively. Color code: green, Au on the staple shell; orange, Au atoms in the Au_{13} core; yellow, sulfur atoms. Other atoms are not shown for clarity.

considerably faster with ammonia present in the system (Figure 2B). It is worth mentioning that the UV−vis spectrum in the presence of $Co(OAc)_2$ and ammonia in Figure 2B almost becomes a decaying curve after ∼60 min (the 400 to 1100 nm range). Other Lewis acids, $NiCl_2$, $Cu(OAc)_2$, $Cu(OAc)_1$, and $Cr(NO_3)_3$ (M^{z+}:$Au_{25}(SR)_{18}$ = 2:1, mol/mol) with ammonia yield essentially the same, albeit slower, temporal evolution of the UV−vis spectrum (Figure 2, parts C and D, and Figure S8). The spectra at 10 min (and at 5 min for Co^{2+}) in Figure 2E show an excellent correlation with the trend of the reaction rate in Table 1, i.e., conversion rate decreases in the order $Co^{2+} > Ni^{2+} \approx Cr^{3+} > Cu^+ > Cu^{2+}$. By contrast, $Au_{25}(SR)_{18}$ nanoclusters remain intact when only ammonia is present at 50 °C (Figure S9). These results indicate that ammonia acts as a promoter for the Lewis acid-induced removal of a "—Au—SR—" unit from the parent $Au_{25}(SR)_{18}$ nanoclusters. Additionally, we studied the removal process by MALDI−MS at different reaction times. As shown in Figure 2F, the intensity of the mass peak at m/z 7060 corresponding to the $Au_{24}(SR)_{17}$ species gradually increased, indicating the $Au_{25}(SR)_{18}$ nanoclusters are converted to $Au_{24}(SR)_{17}$ in the presence of Lewis acid. This provides further evidence that the $Au_{24}(SR)_{17}$ species is newly formed, rather than fragments of $Au_{25}(SR)_{18}$ like the $Au_{21}(SR)_{14}$ species.

The mass spectrometry results as well as the data in Table 1 suggest that the catalytic activity is associated with the newly generated $Au_{25-n}(SR)_{18-n}$ species such as $Au_{24}(SR)_{17}$. This means that Lewis acids may be not only directly involved in the hydrogenation reaction, but also responsible for the generation of $Au_{24}(SR)_{17}$ species with active sites for catalysis. As a consequence, a better adsorption of Lewis acids onto the nanoclusters and/or a faster generation of $Au_{24}(SR)_{17}$ would lead to a higher promotion of the hydrogenation reaction (e.g., $Co^{2+} > Cu^{2+}$). In what follows, we consider in detail the structure of $Au_{24}(SR)_{17}$, its production pathways from the parent $Au_{25}(SR)_{18}$ nanoclusters in the presence of a Lewis acid and a base, and potential mechanisms for ensuing hydrogenation reactions.

Structure of $Au_{24}(SR)_{17}$ Species. There are three nonequivalent Au−SR pairs on the $Au_{25}(SR)_{18}$ nanoclusters[10,11] (denoted as Au_{25} NC in Figure 3) that can be removed upon exposure to Lewis acids: two different pairings of Au of a "—SR—Au—SR—" staple motif with —SR (i.e., α and β fragments), and one for Au of the Au_{13}-core (γ pairing). Since the removal of a γ unit from the Au_{13}-core is likely to induce strong disruptions of Au_{25} NC's structure and characteristics (e.g., cluster rearrangement and major electronic property changes), we consider here only the removal of fragments α and β that results in the formation of new species Au_{24} NC-1 (Figure 3B) and Au_{24} NC-2 (Figure 3C), respectively. DFT predicts that the optimized $Au_{24}(SCH_3)_{17}^-$ structure of Au_{24} NC-1 is more stable than that of Au_{24} NC-2 by 21.2 kcal/mol. This is in good agreement with previous studies[10,11,46] and also with our Au—S bond length results (Table S3).

The calculated optical absorption spectra of Au_{25} NC, Au_{24} NC-1, and Au_{24} NC-2 are shown in Figure 3. We considered only the two lowest absorption bands. The maximum intensity lines of these absorption bands of Au_{25} NC are located at 1.72 eV (720 nm) and 2.74 eV (452 nm), consonant with measurements (1.80 and 2.75 eV).[10] Perhaps the most salient aspect of our results is that the lowest absorption band nearly disappears for Au_{24} NC-1, while it remains as a shoulder in the case of Au_{24} NC-2 (Figure 3). The calculated spectrum of Au_{24} NC-1 agrees well with the featureless experimental UV−vis results in Figure 2A−C. It is also possible that the absence of specific band structures in the UV−vis spectra is due to the presence of different complexes. However, in view of TD-DFT as well as the DFT results for the relative stability above, we believe that the structure of the $Au_{24}SR_{17}$ species generated in the solution of Lewis acids is mainly characterized by Au_{24} NC-1 in Figure 3B.

Mechanism of $Au_{24}(SR)_{17}$ Generation. To rationalize the removal mechanism of a "—Au—SR—" pair unit from the $Au_{25}(SCH_3)_{18}^-$ nanoclusters, we investigated possible adsorption sites of a Lewis acid (M^{z+} ion) on $Au_{25}(SCH_3)_{18}^-$ using the
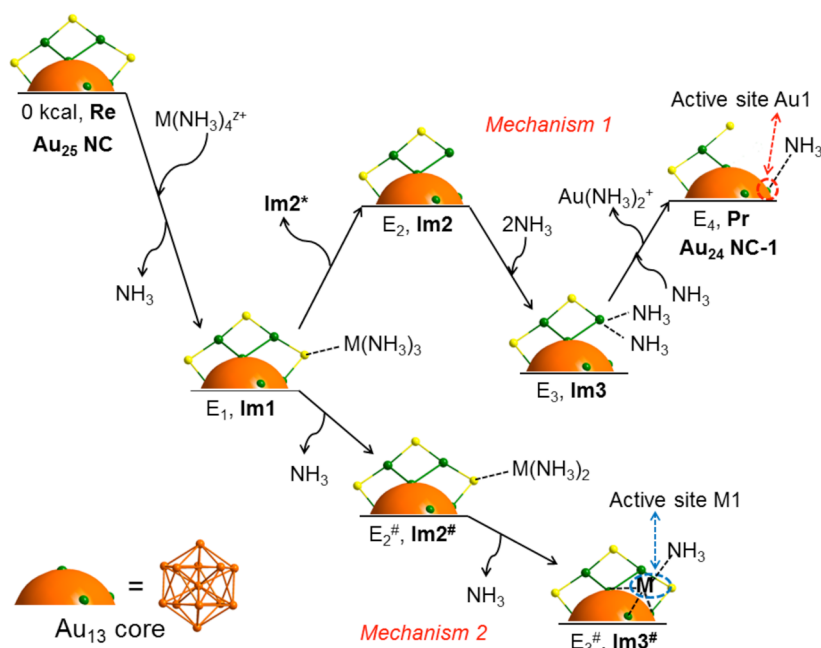
Figure 4. Proposed mechanisms for speciation of $Au_{24}(SR)_{17}$ (*Mechanism 1*) and formation of adduct [nanoparticle-M]$^{(z-1)+}$ (*Mechanism 2*) in the presence of M^{z+} salt and ammonia. A gold atom (Au1) from the Au_{13}-core becomes exposed to the solvent in *Mechanism 1* (upper pathway), while the transition metal ion at M1 becomes an active site in *Mechanism 2* (lower pathway). The calculated energies for different steps are given in Table 3. Color code: Au, green; S, yellow. The orange section represents the Au_{13} core and Im2* denotes $[M(NH_3)_3SCH_3]^{(z-1)+}$.

Table 3. DFT Results for Energies (kcal/mol) for Elementary Steps of *Mechanisms 1 and 2* in Figure 4[a]

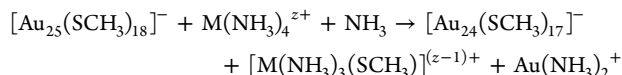|	Cu^+	Cu^{2+}	Ni^{2+}	Co^{2+}
$E_1 = \Delta E(\mathbf{Re} \rightarrow \mathbf{Im1})$	−66.9	−197.6	−188.0	−183.6
$\Delta E(\mathbf{Im1} \rightarrow \mathbf{Im2})$	+60.2	+69.9	+55.2	+42.5
$\Delta E(\mathbf{Im2} \rightarrow \mathbf{Im3})$	−20.8 (~−14)	−20.8 (~−14)	−20.8 (~−14)	−20.8 (~−14)
$\Delta E(\mathbf{Im3} \rightarrow \mathbf{Pr})$	+64.1 (~0)	+64.1 (~0)	+64.1 (~0)	+64.1 (~0)
E_2	−6.7 (~+25)	−127.7 (~+15)	−132.8 (~+14)	−141.1 (~+18)
E_3	−27.5 (~+11)	−148.5 (~+1)	−153.6 (~0)	−161.9 (~+4)
E_4	+36.6 (~+11)	−84.4 (~+1)	−89.5 (~0)	−97.8 (~+4)
$E_2^{\#}$	−59.3			
$E_3^{\#}$	−65.5			

[a]Solution-phase energetics estimated using the IEFPCM and Born solvation free energies are given in parentheses. All energy values are relative to the reactant state **Re**.

DFT method. We considered Cu^+, Cu^{2+}, Ni^{2+}, and Co^{2+} for M^{z+} in the calculations. In *Mechanism 1* (upper pathway in Figure 4), the sulfur atom of unit α (Figure 3) forms a bond with M^{z+} (**Re** → **Im1**). This adsorption process is energetically exothermic in the gas phase by 66.9, 197.6, 188.0, and 183.6 kcal/mol with M^+—S bond length 2.29, 2.30, 2.36, and 2.45 Å for Cu^+, Cu^{2+}, Ni^{2+}, and Co^{2+}, respectively (Table 3). In aqueous solution, the exothermicity is expected to decrease due to the solvation stabilization of the charged reactants. (For insight into solvation effects, the IEFPCM results for solution-phase energetics are given in Table 3 and in Table S4). For clarity, we mention that the coordination number (CN) was assumed to be 4 for the isolated metal complex, i.e., $M(NH_3)_4^{z+}$, and one of the four NH_3 moieties was assumed to be displaced from the coordination shell as the complex attaches itself to the cluster. As a result, the Lewis acid (M^{z+} ion) adsorbed on the cluster surface is coordinated to three NH_3 molecules. Although we do not exclude possibilities of CN higher or lower than 4 for the isolated metal complex, our results for CN = 4 clearly show that a considerable amount of energy is released with the formation of a M^{z+}—S bond. This excess energy can facilitate the removal of the entire M^{z+}—S moiety (**Im2***), i.e., thiolate group plus metal complex, from the gold nanocluster and thus the formation of $Au_{25}(SCH_3)_{17}$ (**Im1** → **Im2**). The removal of M^{z+}—S is an endothermic process with $\Delta E = +60.2, + 69.9, + 55.2$, and +42.5 kcal/mol for Cu^+, Cu^{2+}, Ni^{2+}, and Co^{2+}, respectively. We parenthetically note that ΔE for **Im1** → **Im2** in the gas phase decreases in the order $Cu^{2+} > Cu^+ > Ni^{2+} > Co^{2+}$, in concert with the experimental trend of the conversion rate of hydrogenation (Table 1). One potential explanation is that the thiolate group removal is a key step of the hydrogenation reaction.

The resulting nanoclusters $Au_{25}(SCH_3)_{17}$ have a gold atom that is bonded to only one thiolate group. Two ammonia (NH_3) molecules can coordinate to this gold atom exothermically with the Au—N distance of 2.39 Å and energy release of 20.8 kcal/mol (**Im2** → **Im3**). The coordinating NH_3 molecules eventually detach the gold atom from the nanocluster, resulting in the formation of $Au(NH_3)_2^+$ and $Au_{24}(SCH_3)_{17}^-$ (**Im3** → **Pr**, Figure 4). While the final step is endothermic by +64.1 kcal/mol in the gas phase, endothermicity becomes negligible in aqueous solutions because of significant solvation stabiliza-

tion of the charged products. The overall reaction of the inorganic complex with the gold nanoclusters based on *Mechanism 1* can be written as follows:

$$[Au_{25}(SCH_3)_{18}]^- + M(NH_3)_4{}^{z+} + NH_3 \rightarrow [Au_{24}(SCH_3)_{17}]^-$$
$$+ [M(NH_3)_3(SCH_3)]^{(z-1)+} + Au(NH_3)_2{}^+$$

with ΔE= +36.6, −84.4, −89.5, and −97.8 kcal/mol (gas-phase) and ~11, ~1, ~0, and ~4 kcal/mol (solution-phase) for Cu^+, Cu^{2+}, Ni^{2+}, and Co^{2+}, respectively.

Mechanism 1 proposed here explains our experimental finding that the presence of base $NH_3 \cdot H_2O$ accelerates the disappearance of the absorption band at ~670 nm (Figure 2, parts A vs B). NH_3 is usually a better lone-pair donor than CH_3OH to coordinate and form a complex with Au. Similarly, it can also explain another experimental finding above, i.e., NH_3 leads to a higher conversion than pyridine (see Hydrogenation Mechanism below), in that NH_3 is a better lone-pair donor than pyridine to coordinate to gold.

We briefly pause here for perspective. While our DFT (and UV−vis) results indicate that Au_{24} NC-1 (Figure 3B) is the dominant configuration of $Au_{24}SR_{17}$ species generated in the solution of Lewis acids, the effect of the CeO_2 support was not accounted for in the calculations. CeO_2 can play a crucial role to, for example, rearrange the structure of the nanoparticles and change the active sites. Therefore, even if the direct generation of Au_{24} NC-2 from its parent Au_{25} NC via removal of a β unit may be suppressed (see Figure 3 above), it can be produced from Au_{24} NC-1 via, e.g., ligand exchange[47] on the support. The formation of Au_{24} NC-2 yields an active gold site (Au2) on a staple motif rather than on the core (see Figure S10).

Mechanism of the Adduct [nanoparticle-M]$^{(z-1)+}$ Formation. In *Mechanism 2*, i.e., the lower pathway in Figure 4, a considerable energy release via M^{z+}—S bond formation (**Re** → **Im1**) can result in the removal of coordinating ammonia molecules (**Im1** → **Im2$^{\#}$** → **Im3$^{\#}$**) rather than the interacting thiolate group. ΔE for **Im1** → **Im2$^{\#}$** and **Im2$^{\#}$** → **Im3$^{\#}$** steps are +7.6 and −6.2 kcal/mol, respectively, for M^{z+} = Cu^+. As illustrated in Figure 4, M^{z+} becomes adsorbed on the Au_{13}-core surface by coordinating to three core Au atoms (**Im3$^{\#}$**). This in turn can induce a considerable elongation (0.05 Å) of nearby Au—S bonds, exposing their thiolate groups even more to the Lewis acids in the solvent. Therefore, it is also possible that **Im3$^{\#}$** follows the pathway of *Mechanism 1* discussed above, i.e., **Im3$^{\#}$** → **Im2** → **Im3** → **Pr**, by losing one of the "—Au—SR—" pair units ($\Delta E = E_{Pr} - E_{Im3}{}^{\#} = +102.1$ kcal/mol).

The net charge of Au_{25} NC in the present study was −1. Since the charge state of nanoclusters can modulate their solvation energy and spin multiplicity, it could exert a considerable influence on reaction kinetics and thermodynamics of the Au-SR removal (*Mechanism 1*) and/or adduct formation (*Mechanism 2*). For example, we expect that the solvation effect on overall reaction thermodynamics of the adduct formation would vary significantly with the charge state because the reactant and product nanocluster states, i.e., Au_{25} NC and **Im3$^{\#}$** of *Mechanism 2*, are characterized by different electric charges. By contrast, in the case of *Mechanism 1*, the corresponding change of the solvation effect with the charge state would not be as significant because Au_{25} NC and Au_{24} NC-1 have the same charge. It would thus be both interesting and worthwhile to study in the future how the charge state of

nanoclusters influences their catalytic activity in hydrogenation reactions.

Hydrogenation Mechanism. Since essentially all surface gold atoms of $Au_{25}(SC_2H_4Ph)_{18}{}^-$ are protected by thiolate groups, the Au_{25} NC nanoclusters are inert toward adsorption of nonradical molecules on their surface.[48,49] Our calculations indeed show that there are no strong interactions of $Au_{25}(SCH_3)_{18}{}^-$ with possible adsorbates (e.g., PhCHO, NH_3, and H_2), in accordance with recent theoretical studies.[48,49] However, the removal of an Au-SR fragment or the formation of an adduct exposes open metal atoms (a gold atom of the core Au_{13} or on staple motifs, or the Lewis acids) to the solvent (Figures 4 and S10). DFT predicts that these sites, i.e., Au1, Au2, and M1 in Figures 4 and S10, are active toward adsorption of reactants. In view of these results, we propose hydrogenation mechanisms (Figure 5), in which bond activation of H_2 on these metal sites is the first step.

Upon removal of the capping NH_3 from the metal site (Au1, Au2, or M1), the H—H bond of a H_2 molecule becomes activated with the aid of a base (Figure 5). Specifically, the base (NH_3) abstracts a proton from H_2 to form $NH_4{}^+$ with H^- on the active metal site (**Re*^{Au1} → Im1*^{Au1}, Re*^{M} → Im1*^{M}, Re*^{Au2} → Im1*^{Au2}**). The removal of capping NH_3 and adsorption of a H_2---NH3 unit are endothermic and exothermic, respectively. Overall, this two-step process at the Au1 and M1 active sites is endothermic by +4.9 and +19.7 kcal/mol, respectively. For Au2, this step is found to be exothermic by 3.5 kcal/mol. In a polar solvent like water, however, the product state would become considerably stabilized compared to the reactant because of the highly charge-separated nature of the $NH_4{}^+$---H^- moiety. DFT calculations indicate that the presence of a base, such as NH_3, is crucial for the activation of H_2. Without a base, the interaction of H_2 with M1 and Au2 is mainly physical and that with Au1 is rather weak, so that H_2 tends to stay away from Au1. Thus, a base is needed for chemical adsorption of H_2 and ensuing H—H bond activation on Au1 and M1. This participation of a base in the H_2 activation as well as in the removal of a gold atom discussed above (*Mechanism 1*) provides a theoretical explanation for our experimental findings that no hydrogenation reaction occurred in the absence of a base and that a stronger base (NH_3 vs. pyridine) yields a higher conversion efficiency (Table S2). Of note, the lone-pair on nitrogen is in sp^3 and sp^2 orbitals in the cases of NH_3 and pyridine, respectively. In the case of the Au1 active site, PhCHO becomes physically adsorbed on the surface of the nanoclusters via interactions of its O and C (—CHO group) with $NH_4{}^+$ and H^-, respectively, in an exothermic step with $\Delta E = −5.3$ kcal/mol (**Im1*^{Au1} → Im2*^{Au1}**, Figure 5A). Finally, H^+ (of $NH_4{}^+$) and H^- will transfer to PhCHO and produce $PhCH_2OH$ exothermically with energy release of 15.4 kcal/mol (**Im2*^{Au1} → Re*^{Au1}**, Figure 5A).

In the case of hydrogenation catalyzed by the M1 and Au2 sites (Figure 5, parts B and C), the ammonium ion formed (**Im1*^{M}** and **Im1*^{Au2}**) may become solvated in the reaction media and act as a donor for protonation of aldehyde (**Im1*^{M} → Im2*^{M}** and **Im1*^{Au2} → Im2*^{Au2}**). For M1 and Au2, this step is found to be endothermic by +26.0 and +46.8 kcal/mol in water, respectively, while it is +111.6 and +158.4 kcal/mol in the gas phase. Since the products, $NH_4{}^+$, $Au_{25}SR_{18}CuH^-$, and $Au_{24}SR_{17}H^{2-}$ are charged, they are strongly stabilized in water, compared to the gas phase (see Table S4). This means that solvation can facilitate (or even induce) the elongation of the H—H bond (g in Figure 5B) to produce charged species
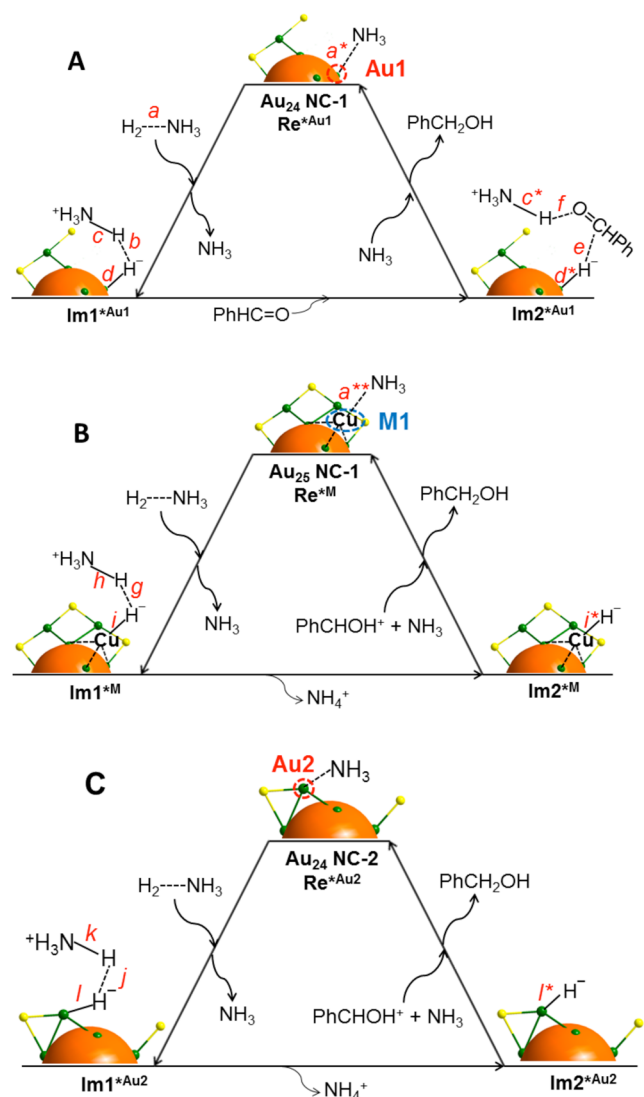
Figure 5. Proposed mechanism for hydrogenation of benzaldehyde in the presence of H_2 and NH_3 on (A) site Au1, (B) site M1, and (C) site Au2. The values of interatomic distances are $a^* = 2.26$, $a = 2.56$, $b = 1.82$, $c = 1.05$, $d = 1.64$, $c^* = 1.03$, $d^* = 1.63$, $e = 2.85$, $f = 1.87$, $a^{**} = 2.03$, $g = 0.80$, $h = 2.04$, $i = 1.74$, $i^* = 1.53$, $j = 1.73$, $k = 1.04$, $l = 1.61$, and $l^* = 1.59$ Å. (For comparison, the equilibrium bond length of an isolated H_2 molecule is 0.74 Å.) The same color code is used as in Figure 4.

(NH_4^+ and H^-). This is followed by the reduction of protonated benzaldehyde to benzyl alcohol (**Im2*M → Re*M** and **Im2*Au2 → Re*Au2**, Figure 5, parts B and C). This final reduction step is exothermic with $\Delta E = -152.1$ and -175.6 kcal/mol, respectively, for the M1 and Au2 sites in the gas phase, while -89.3 and -86.8 kcal/mol in the solution phases.

CONCLUSIONS

The $Au_{25}(SR)_{18}/CeO_2$ catalyst in the presence of a Lewis acid and a base (ammonia or pyridine) exhibits good catalytic performance, including catalytic activity and selectivity, in the aldehyde hydrogenation reactions. The presence of Lewis acids in solution leads to a significant enhancement in the catalytic activity of $Au_{25}(SR)_{18}/CeO_2$ nanoclusters. Among all Lewis acids we studied, Co^{2+} yields the best catalytic conversion. New nanocluster species $Au_{25-n}(SR)_{18-n}$ ($n = 1-4$) generated during

the process were characterized by MALDI/ESI mass spectrometry in conjunction with UV–vis absorption spectroscopy. DFT predicts that the optimized structure of $Au_{24}(SCH_3)_{17}^-$ in the Au_{24} NC-1 configuration is 21.2 kcal/mol more stable than that in the Au_{24} NC-2 configuration. The optical absorption spectrum of the former calculated via TD-DFT shows a good agreement with the experimental results. On the basis of these observations, the mechanism of the removal of a "—Au—SR—" fragment to produce $Au_{24}(SR)_{17}$ from the $Au_{25}(SR)_{18}$ parent nanoclusters in the presence of Lewis acids (e.g., Cu^+, Cu^{2+}, Ni^{2+}, and Co^{2+}) and ammonia is proposed. DFT results further indicate that the surface gold atoms on the Au_{13}-core or staple shell, or the Lewis acids bound on the Au_{13}-core can provide catalytic active sites for hydrogenation. On the basis of experimental and DFT results, we elucidated the hydrogenation mechanism of reducing aldehyde to alcohol. The catalytic hydrogenation is also applied to a range of benzaldehyde derivatives, and the gold nanoclusters catalyst with Lewis acid shows good catalytic activity. While our study reported here contributes novel insights on aldehyde hydrogenation catalyzed by Au nanoclusters, some aspects were not properly accounted for in our computational analysis. These include the molecular aspect of the solvent environment and the role of the CeO_2 support. The latter can modulate the electronic and structural and thus catalytic properties of the gold nanoclusters significantly. Therefore, it would be worthwhile in the future to extend the current study to investigate details of molecular interactions between the nanoparticles and supports and their influence on catalytic efficiency and pathways for hydrogenation and other reactions catalyzed by gold nanoparticles.

■ ASSOCIATED CONTENT

ⓢ Supporting Information

The Supporting Information is available free of charge on the ACS Publications website at DOI: 10.1021/jacs.5b07716.

Thermal stability test of the unsupported $Au_{25}(SR)_{18}$ nanoclusters and the $Au_{25}(SR)_{18}/CeO_2$ catalyst, blank reaction results, MADLI mass spectrum of the $Au_{25}(SC_2H_4Ph)_{18}$ nanoclusters, experimental and simulated isotopic distribution patterns of $Au_{25-n}(SR)_{18-n}$ (n: 1–4) nanoclusters, NMR Data, and stabilization energy of different species in solution with respect to the gas phase, etc. (PDF)

■ AUTHOR INFORMATION

Corresponding Authors
*rongchao@andrew.cmu.edu
*hjkim@cmu.edu

Author Contributions
§G.L. and H.A. contributed equally to this work.

Notes
The authors declare no competing financial interest.

■ REFERENCES

(1) Yamazoe, S.; Koyasu, K.; Tsukuda, T. *Acc. Chem. Res.* **2014**, *47*, 816–824.

(2) Taketoshi, A.; Haruta, M. *Chem. Lett.* **2014**, *43*, 380–387.

(3) Qian, H.; Zhu, M.; Wu, Z.; Jin, R. *Acc. Chem. Res.* **2012**, *45*, 1470−1479.

(4) Li, G.; Jin, R. *Acc. Chem. Res.* **2013**, *46*, 1749−1758.

(5) Boronat, M.; Leyva-pérez, A.; Corma, A. *Acc. Chem. Res.* **2014**, *47*, 834−844.

(6) Liu, J.; Krishna, K. S.; Losovyj, Y. B.; Chattopadhyay, S.; Lozova, N.; Miller, J. T.; Spivey, J. J.; Kumar, C. S. S. R. *Chem. - Eur. J.* **2013**, *19*, 10201−10208.

(7) Shivhare, A.; Ambrose, S. J.; Zhang, H.; Purves, R. W.; Scott, R. W. J. *Chem. Commun.* **2013**, *49*, 276−278.

(8) Li, G.; Jin, R. *J. Am. Chem. Soc.* **2014**, *136*, 11347−11354.

(9) Li, G.; Liu, C.; Jin, R. *Chem. Commun.* **2012**, *48*, 12005−12007.

(10) Zhu, M.; Aikens, C. M.; Hollander, F. J.; Schatz, G. C.; Jin, R. *J. Am. Chem. Soc.* **2008**, *130*, 5883−5885.

(11) Heaven, M. W.; Dass, A.; White, P. S.; Holt, K. M.; Murray, R. W. *J. Am. Chem. Soc.* **2008**, *130*, 3754−3755.

(12) Li, G.; Jiang, D.; Liu, C.; Yu, C.; Jin, R. *J. Catal.* **2013**, *306*, 177−183.

(13) Li, G.; Jiang, D.; Kumar, S.; Chen, Y.; Jin, R. *ACS Catal.* **2014**, *4*, 2463−2469.

(14) Tlahuice-Flores, A.; Whetten, R. L.; Jose-Yacaman, M. *J. Phys. Chem. C* **2013**, *117*, 20867−20875.

(15) Aikens, C. M. *J. Phys. Chem. A* **2009**, *113*, 10811−10817.

(16) Pan, M.; Brush, A. J.; Pozun, Z. D.; Ham, H. C.; Yu, W.; Henkelman, G.; Hwang, G. S.; Mullins, C. B. *Chem. Soc. Rev.* **2013**, *42*, 5002−5013.

(17) Yamane, Y.; Liu, X.; Hamasaki, A.; Ishida, T.; Haruta, M.; Yokoyama, T.; Tokunaga, M. *Org. Lett.* **2009**, *11*, 5162−5165.

(18) Corma, A.; Serna, P. *Science* **2006**, *313*, 332−334.

(19) Cano, I.; Chapman, A. M.; Urakawa, A.; van Leeuwen, M. *J. Am. Chem. Soc.* **2014**, *136*, 2520−2528.

(20) Ren, D.; He, L.; Yu, L.; Ding, R.; Liu, Y.; Cao, Y.; He, H.; Fan, K. *J. Am. Chem. Soc.* **2012**, *134*, 17592−17598.

(21) Zhu, Y.; Qian, H.; Drake, B. A.; Jin, R. *Angew. Chem., Int. Ed.* **2010**, *49*, 1295−1298.

(22) Li, G.; Zeng, C.; Jin, R. *J. Am. Chem. Soc.* **2014**, *136*, 3673−3679.

(23) Zhang, G.; Vasudevan, K. V.; Scott, B. L.; Hanson, S. K. *J. Am. Chem. Soc.* **2013**, *135*, 8668−8681.

(24) Rösler, S.; Obenauf, J.; Kempe, R. *J. Am. Chem. Soc.* **2015**, *137*, 7998−8001.

(25) Gärtner, D.; Welther, A.; Rad, B. R.; Wolf, R.; von Wangelin, A. J. *Angew. Chem., Int. Ed.* **2014**, *53*, 3722−3726.

(26) Zhang, G.; Scott, B. L.; Hanson, S. K. *Angew. Chem., Int. Ed.* **2012**, *51*, 12102−12106.

(27) Mertens, P. G. N.; Wahlen, J.; Ye, X.; Poelman, H.; De Vos, D. E. *Catal. Lett.* **2007**, *118*, 15−21.

(28) Mertens, P. G. N.; Vandezande, P.; Ye, X.; Poelman, H.; Vankelecom, I. F. J.; De Vos, D. E. *Appl. Catal., A* **2009**, *355*, 176−183.

(29) Becke, A. D. *Phys. Rev. A: At., Mol., Opt. Phys.* **1988**, *38*, 3098−100.

(30) Becke, A. D. *J. Chem. Phys.* **1993**, *98*, 5648−5652.

(31) Burant, J. C.; Scuseria, G. E.; Frisch, M. J. *J. Chem. Phys.* **1996**, *105*, 8969−8972.

(32) Frisch, M. J.; Trucks, G. W.; Schlegel, H. B.; Scuseria, G. E.; Robb, M. A.; Cheeseman, J. R.; Scalmani, G.; Barone, V.; Mennucci, B.; Petersson, G. A.; Nakatsuji, H.; Caricato, M.; Li, X.; Hratchian, H. P.; Izmaylov, A. F.; Bloino, J.; Zheng, G.; Sonnenberg, J. L.; Hada, M.; Ehara, M.; Toyota, K.; Fukuda, R.; Hasegawa, J.; Ishida, M.; Nakajima, T.; Honda, Y.; Kitao, O.; Nakai, H.; Vreven, T.; Montgomery, J. A., Jr.; Peralta, J. E.; Ogliaro, F.; Bearpark, M.; Heyd, J. J.; Brothers, E.; Kudin, K. N.; Staroverov, V. N.; Kobayashi, R.; Normand, J.; Raghavachari, K.; Rendell, A.; Burant, J. C.; Iyengar, S. S.; Tomasi, J.; Cossi, M.; Rega, N.; Millam, N. J.; Klene, M.; Knox, J. E.; Cross, J. B.; Bakken, V.; Adamo, C.; Jaramillo, J.; Gomperts, R.; Stratmann, R. E.; Yazyev, O.; Austin, A. J.; Cammi, R.; Pomelli, C.; Ochterski, J. W.; Martin, R. L.; Morokuma, K.; Zakrzewski, V. G.; Voth, G. A.; Salvador, P.; Dannenberg, J. J.; Dapprich, S.; Daniels, A. D.; Farkas, Ö.; Foresman, J. B.; Ortiz, J. V.; Cioslowski, J.; Fox, D. J. Gaussian, Inc., Wallingford CT, 2009.

(33) Dunning, T. H., Jr. *J. Chem. Phys.* **1989**, *90*, 1007−1023.

(34) Fuentealba, P.; Preuss, H.; Stoll, H.; Szentpály, L. V. *Chem. Phys. Lett.* **1982**, *89*, 418−422.

(35) Igel-Mann, G.; Stoll, H.; Preuss, H. *Mol. Phys.* **1988**, *65*, 1321−1328.

(36) Hay, P. J.; Wadt, W. R. *J. Chem. Phys.* **1985**, *82*, 299−310.

(37) Assadollahzadeha, B.; Schwerdtfegera, P. *J. Chem. Phys.* **2009**, *131*, 064306.

(38) Taketsugu, T.; Lyalin, A. *J. Phys. Chem. Lett.* **2010**, *1*, 1752−1757.

(39) Faza, O. N.; Rodríguez, R. Á.; López, C. S. *Theor. Chem. Acc.* **2011**, *128*, 647−661.

(40) Zubarev, D. Y.; Boldyrev, A. I. *J. Phys. Chem. A* **2009**, *113*, 866−868.

(41) Scalmani, G.; Frisch, M. J. *J. Chem. Phys.* **2010**, *132*, 114110−114115.

(42) Haruta, M.; Tsubota, S.; Kobayashi, T.; Kageyama, H.; Genet, M. J.; Delmon, B. *J. Catal.* **1993**, *144*, 175−192.

(43) Chng, L. L.; Erathodiyil, N.; Ying, J. Y. *Acc. Chem. Res.* **2013**, *46*, 1825−1837.

(44) Wu, Z.; Jiang, D.; Mann, A. K.; Mullins, D. R.; Qiao, Z. A.; Allard, L. F.; Zeng, C.; Jin, R.; Overbury, S. H. *J. Am. Chem. Soc.* **2014**, *136*, 6111−6122.

(45) Li, Y.; Shen, W. *Chem. Soc. Rev.* **2014**, *43*, 1543−1574.

(46) Lopez-Acevedo, O.; Hakkinen, H. *Eur. Phys. J. D* **2011**, *63*, 311−314.

(47) Fernando, A.; Aikens, C. M. *J. Phys. Chem. C* **2015**, *119*, 20179−20187.

(48) Lopez-Acevedo, O.; Kacprzak, K. A.; Akola, J.; Häkkinen, H. *Nat. Chem.* **2010**, *2*, 329−334.

(49) Liu, C.; Lin, S.; Pei, Y.; Zeng, X. C. *J. Am. Chem. Soc.* **2013**, *135*, 18067−18079.